Research article

Mel F. Hainey, Jr.*, Takaaki Mano, Takeshi Kasaya, Tetsuyuki Ochiai, Hirotaka Osato, Kazuhiro Watanabe, Yoshimasa Sugimoto, Takuya Kawazu, Yukinaga Arai, Akitsu Shigetou and Hideki T. Miyazaki*

Systematic studies for improving device performance of quantum well infrared stripe photodetectors

https://doi.org/10.1515/nanoph-2020-0095
Received February 7, 2020; accepted June 4, 2020; published online July 4, 2020

Abstract: The integration of quantum well infrared photodetectors with plasmonic cavities has allowed for demonstration of sensitive photodetectors in the mid-infrared up to room-temperature operating conditions. However, clear guidelines for optimizing device structure for these detectors have not been developed. Using simple stripe cavity detectors as a model system, we clarify the fundamental factors that improve photodetector performance. By etching semiconductor material between the stripes, the cavity resonance wavelength was expected to blue-shift, and the electric field was predicted to strongly increase, resulting in higher responsivity than unetched stripe detectors. Contrary to our predictions, etched stripe detectors showed lower responsivities, indicating surface effects at the sidewalls and reduced absorption. Nevertheless, etching led to higher detectivity due to significantly reduced detector dark current. These results suggest that etched structures are the superior photodetector design, and that appropriate sidewall surface treatments could further improve device performance. Finally, through polarization and incidence angle dependence measurements of the stripe detectors, we clarify how the design of previously demonstrated wired patch antennas led to improved device performance. These results are widely applicable for cavity designs over a broad range of wavelengths within the infrared, and can serve as a roadmap for improving next-generation infrared photodetectors.

Keywords: etching; infrared photodetector; intersubband transition; metasurface; plasmonic cavity; quantum well.

1 Introduction

Photodetectors operating in the mid-infrared range are widely used for chemical detection, remote sensing, and imaging technologies. However, current detectors for wavelengths greater than 5 μm are based on highly toxic and difficult to fabricate mercury cadmium telluride (HgCdTe) alloys [1, 2]. One alternative structure receiving increased attention is a photodetector based on quantum wells integrated with plasmonic metasurfaces, which we call a metasurface quantum well infrared photodetector (metasurface QWIP) [3–6]. This type of detector uses less toxic and standard semiconductor industry materials, and is fabricated with well-established processes. Additionally, both the quantum well [7, 8] and metasurface [9–11] can be independently tuned over a wide range of wavelengths.

Plasmonic metasurface cavities consist of two metal layers, typically Au, sandwiching a thin dielectric material. Vertically (z) incident light with an electric field parallel to the cavity surface (E_x) is rotated into the normal direction (E_z) through magnetic coupling (H_y) with the cavity. Due to confinement within the cavity, the magnitude of the electric field is dramatically enhanced [12]. A single cavity can absorb light across a much larger area than its physical area [12–14], and the plasmon resonance

***Corresponding authors: Mel F. Hainey and Hideki T. Miyazaki,** National Institute for Materials Science, Tsukuba, Ibaraki 305-0047, Japan, E-mail: HAINEYJR.Mel@nims.go.jp (M. F. Hainey); MIYAZAKI.Hideki@nims.go.jp (H. T. Miyazaki). https://orcid.org/0000-0003-3878-099X (Mel F. Hainey).
Takaaki Mano, Takeshi Kasaya, Tetsuyuki Ochiai, Hirotaka Osato, Kazuhiro Watanabe, Yoshimasa Sugimoto, Takuya Kawazu, Yukinaga Arai and Akitsu Shigetou: National Institute for Materials Science, Tsukuba, Ibaraki 305-0047, Japan, E-mail: mano.takaaki@nims.go.jp (T. Mano), kasaya.takeshi@nims.go.jp (T. Kasaya), ochiai.tetsuyuki@nims.go.jp (T. Ochiai), oosato.hirotaka@nims.go.jp (H. Osato), qqyr7t89@sunny.ocn.ne.jp (K. Watanabe), sugimoto.yoshimasa@nims.go.jp (Y. Sugimoto), kawazu.takuya@nims.go.jp (T. Kawazu), arai.yukinaga@nims.go.jp (Y. Arai), shigetou.akitsu@nims.go.jp (A. Shigetou)

wavelength can be adjusted across a broad range of wavelengths by simply changing the cavity dimensions [10]. These properties have been previously used for perfect absorbers [14, 15] and plasmonic metasurface cavity thermal emitters [16–18].

The electric field rotation and enhancement make metasurface cavities particularly attractive for integration with QWIPs. These detectors operate based on engineered intersubband transitions (ISBT) of electrons within the conduction band of the quantum well [19], where the transition energy corresponds to a desired wavelength in the infrared, and generate a photoconductive current by applying a bias voltage. Due to ISBT selection rules, only light with an electric field normal to the quantum well surface (E_z) can be absorbed, leading to low absorption in standard QWIP architectures using a 45° etched facet or integrated diffraction gratings [7]. In a metasurface QWIP, however, the cavities provide rotation and an enhanced field to generate strongly enhanced absorption. Provided the resonance wavelength of the metasurface cavity is matched to the absorption peak of the QWIP, the sensitivity of the QWIP to radiation at normal incidence is greatly enhanced. Additionally, the metallic layers of the cavity can be used as electrodes, allowing for straightforward biasing and carrier collection from the quantum wells [20].

An initial report by Chen et al. demonstrated metasurface QWIPs with square patches connected by thin wires [3]. Most importantly, they reported that removing semiconductor material from outside the cavity area reduced the detector dark current (I_D), the current present in a detector under bias due to its inherent transport properties. The background current (I_{BG}), the baseline current inevitable during normal operation in a detector under bias due to radiation from a room temperature (300 K) environment, barely changed after etching, indicating that light absorption was largely unaffected. This was reported to allow an increase in the detector operating temperature due to an increased I_{BG}/I_D ratio. Based on this report, modified versions of the etched, wired patch structures were later used to demonstrate room-temperature detector operation [5, 6].

However, these results left questions unanswered regarding fundamental metasurface QWIP behavior. While Chen et al. showed that dry etching reduced I_D in the detector [3], they did not discuss how etching would affect the detector responsivity (R), the output current generated per unit of incident power. Because the change in the magnitude of R due to dry etching was not shown, improvement in the detectivity (D^*), the signal-to-noise ratio described by R and I_D and the most fundamental figure of merit in infrared photodetectors, could not be clarified. Dry etching was also reported to blue-shift the plasmon resonance peak of the metasurface QWIP, but only minimal explanation was given for this behavior. There was no systematic study performed to clarify the mechanism of this blue-shift. Finally, wiring-induced changes in photoresponse such as polarization-dependence [5] and absorption peak position shifts [6] in wired patch antenna structures make fundamental analysis of device performance difficult.

For studying fundamental metasurface QWIP behavior, a simple stripe structure offers a clearer physical picture and allows for more straightforward comparison with previously developed physical models [21–25]. This structure also allows for simple electrical contacting because stripes can easily be connected to a larger metal contact pad. Stripe metasurface QWIPs have been previously studied [4] as high-polarization-discriminating detectors, but the thick QWIP structure in the report had a complex optical response with multiple plasmon resonance modes (third-order Fabry–Perot mode and surface plasmon mode due to the diffraction) present at different positions in the cavity. Furthermore, there was no discussion on etching of the semiconductor to improve I_D and D^*.

In this report, we systematically study etched and unetched stripe metasurface QWIP performance. Both types of detector are fabricated from an identical, well-characterized quantum well, so that only the final dry etching step defines the different morphology of stripes. The effect of etching on metasurface QWIP resonance peak position and photoresponse is systematically demonstrated, along with its effect on I_D and D^*. Electromagnetic simulation predicts higher R for etched structures due to the enhanced fields in the cavities. However, experiments actually gives lower R for etched cavities; this unexpected results shows that device performance cannot be predicted simply by cavity shape, and the effects of the surfaces at the etched sidewalls due to the processing must also be considered. Nonetheless, etched stripes are found to be the superior structure with higher D^* due to their reduced I_D. Surface effects such as depletion layers and etching damage have been considered insignificant for conventional QWIPs [26], but may have greater impact on metasurface QWIP performance because absorption is strongest at the cavity sidewalls and the etched surface areas are much larger. Appropriate sidewall surface treatments could therefore lead to further improvement in etched detector performance. These results give a comprehensive picture of how cavity morphology determines metasurface QWIP behavior, providing a roadmap for future development of detectors with optimum photoresponse and detectivity.

2 Results and discussion

To understand the effects of etching on metasurface behavior, we begin with the simple metal/dielectric/metal structures illustrated in Figure 1A, B. A single unit of a stripe array has length L and period P, with a dielectric layer thickness of T = 200 nm. The top and bottom metal layers are made of Au, and have thicknesses of t_{m1} = 100 nm and t_{m2} = 200 nm respectively. For etched structures, both the top Au layer and dielectric have length L, while for the unetched structure, only the top Au layer has a length of L. The dielectric constant of Au is taken from Ordal et al. [27]. The dielectric layer was assumed to be homogenous and nondispersive, and the refractive index for the dielectric was taken as n = 3.05 + 0.10i, based on preliminary experiments involving the actual GaAs/AlGaAs quantum well structures used later in the manuscript. Incident light was assumed to be normal to the detector with x polarization. Using rigorous coupled wave analysis (RCWA), and assuming initial L value of 1.0 μm, we can realize total absorption at 7.00 μm with P = 2.3 μm for an etched structure (Figure 1C). However, for an unetched structure with the same L and P, the absorption peak is red-shifted to 8.17 μm while keeping nearly unity absorption. Therefore, for absorption at the same wavelength, L must be smaller for an unetched structure than for an etched structure. This is similar to the behavior observed in Chen et al. where a 1.4 μm etched square cavity was reported to have the same resonance peak as 1.1 μm unetched cavity [3]. Note that for normal incidence with y polarization, no absorption peak appears for either structure, indicating strong polarization-dependence [4]. Here polarization angle (φ) is defined as the angle relative to the x axis (φ = 0° for x and φ = 90° for y polarization).

To understand the origins of this peak shift, electromagnetic fields were investigated. The intensity of the z component electric field ($|E_z|^2$) was calculated for both structures at z = 0.1 μm, corresponding to the center of the dielectric where the quantum well is located (Figure 1D), and the distributions of $|E_z|^2$ over a single period P were mapped (Figure 1E, F). The normal incident electric field intensity is taken as 1. For both structures, the cavity supports a half-wave Fabry–Perot resonance of the metal/dielectric/metal waveguide mode by the reflection at the both edges of the cavities. As seen in Figure 1E, for the

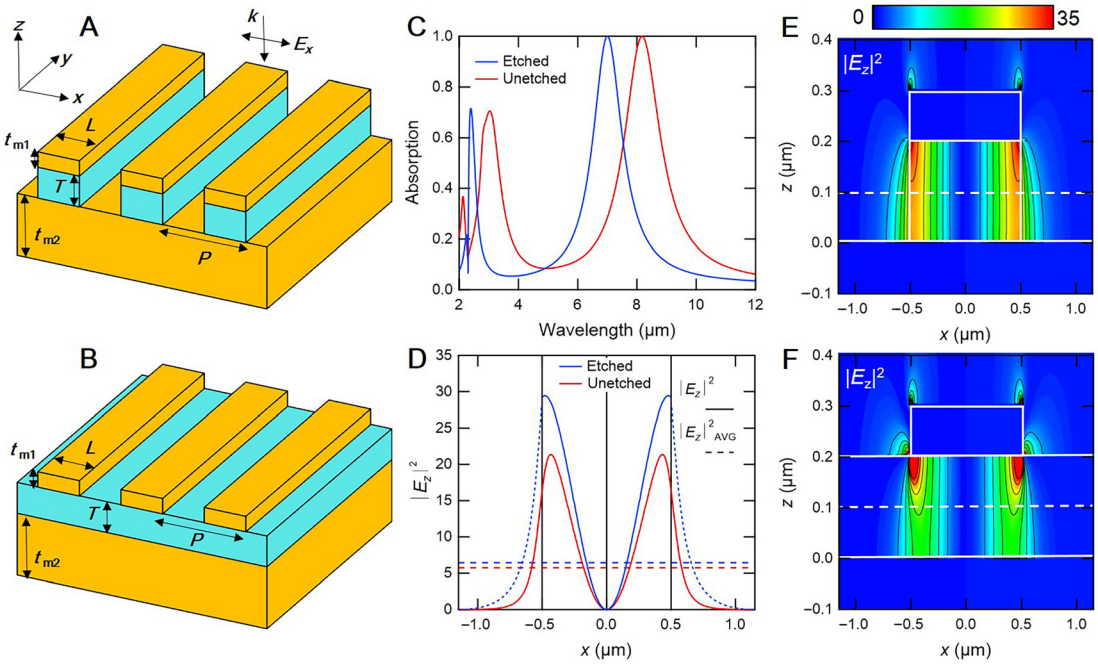

Figure 1: Modeling of stripe cavity structure. A, B) Schematics of etched and unetched structures. ***k*** and ***E*** indicate the incidence direction and polarization of incoming light. C) Simulated absorption profiles for both structures with L = 1.0 μm and P = 2.3 μm. D) Magnitude and average values for $|E_z|^2$ within one period P for each structure taken at z = 0.1 μm, normalized to the incident field. Note dotted areas of the etched curve (blue) indicate regions with no semiconductor material. E, F) Color maps of $|E_z|^2$ for entire period P for etched and unetched structures. White lines indicate the cavity shape, with the dashed line indicated the position of the quantum well. Contour lines are taken at every increase of five in intensity (5, 10, … ,35).

etched stripes, $|E_z|^2$ has a high, uniform magnitude across the thickness T of the dielectric, particularly near the edges of the cavity, which suggests strong reflection of the waveguide mode at the ends. This arises from the mismatch between refractive indices (impedance mismatch) of the metal/dielectric/metal waveguide and the surrounding ambient. Note that compared to $|E_z|^2$, $|E_x|^2$ within the cavity is significantly smaller. At infrared wavelengths, the effective index of the metal/dielectric/metal waveguide can be reasonably approximated by [16, 22]

$$n_{\text{eff}} = n_{\text{r}}\sqrt{1+\frac{2\delta}{T}}, \tag{1}$$

where n_{r} is the real part of the refractive index of the dielectric and δ is the skin depth of the metal, 22 nm for Au [27]. Based on this model, we obtain $n_{\text{eff}} = 3.17$, which has a significant index mismatch with the surrounding ambient ($n = 1$). However, for the unetched stripes (Figure 1F), the index mismatch between the metal/dielectric/metal stack and the surrounding dielectric is much smaller ($n_{\text{eff}} = 3.17$ vs. $n_{\text{r}} = 3.05$), so the reflection is not as strong. The weaker reflection leads to distorted distribution of $|E_z|^2$ that is localized at the corners of the metal stripes but does not extend deeply into the dielectric layer. Also, the incomplete reflection phase makes the effective cavity length longer than the geometrical length of the metal/dielectric/metal waveguide [21, 24, 25]. Thus, for resonance at the same wavelength, L must be smaller for an unetched structure than for an etched structure. Selection of metasurface cavity dimensions corresponding to a desired resonance wavelength will thus strongly depend on the intended cavity morphology.

In considering R, the spatial range of the contributing semiconductor should also be taken into account. While there is no dielectric material to absorb light outside the cavity for the etched stripes, for the unetched stripes, the dielectric outside the stripe cavity will absorb light, contributing to the overall R value of the detector. Although the magnitude of the electric field within the cavity is lower for the unetched stripes, it is not necessarily clear that the total R is inferior to the etched stripes. This can be clearly understood by evaluating the average electric field intensity $|E_z|^2_{\text{AVG}}$ for etched and unetched stripes across the entire period P

$$|E_z|^2_{\text{AVG}} = \frac{\int |E_z|^2 \text{dx}}{P}. \tag{2}$$

For the etched stripe, (2) is integrated only over the cavity length L. For the unetched stripe, it is integrated over the entire period P due to the presence of the dielectric outside the cavity. As seen from the horizontal lines in Figure 1D, while $|E_z|^2_{\text{AVG}}$ for the etched cavities suggests they should have higher responsivities than unetched cavities, the difference is not dramatic but instead relatively small. Therefore, while this simple modeling was convenient to overview the effects of cavity shape, further detailed investigation based on experimental validation and exact modeling is important for clearly determining the optimum structure for a metasurface QWIP structure.

To evaluate how these modeled structures behave experimentally, etched and unetched stripe detectors were fabricated following the processes described in the Section 4. Before designing stripe metasurface QWIP detectors, a Brewster-angle incidence detector was fabricated (see Section 4) to characterize the intrinsic R of the GaAs/AlGaAs quantum well. We obtained a peak unpolarized responsivity (R_{peak}) of 4.1 mA/W at 6.7 μm. Based on the above simulations, stripe detectors were designed to exhibit total absorption peaked at 6.7 μm, and values of L = 0.96 μm and P = 2.4 μm for etched stripes and L = 0.79 μm and P = 2.3 μm for unetched stripes were determined. We also fabricated stripes with L values that gave resonance at wavelengths covering the entire range of the quantum well absorption peak. Scanning electron microscope (SEM) images of both etched and unetched structures can be seen in Figure 2A, B, with the metallic and dielectric regions colored following the schematics in Figure 1A, B. R was evaluated by cooling samples to 78 K and measuring detector current with the detector exposed to radiation from a Fourier transform infrared (FTIR) spectrophotometer. I_{D} and I_{BG} were measured with the detector covered by a cold shield at 78 K or under illumination from a black body surface at 298 K with a field of view of 102°.

From Figure 3A, B, we can compare the experimental responsivity spectra for etched and unetched detectors for a wide range of L values. For comparison, the responsivity of the Brewster-angle detector, characteristic of the quantum well, is shown in Figure 3C. All spectra in Figure 3A–C were taken for unpolarized incident radiation. The responsivity spectra for etched and unetched detectors exhibit envelopes analogous to the responsivity spectrum of the quantum well, peaked at a similar wavelength. Thus the maximum R of metasurface QWIPs is achieved when the cavity resonance peaks are in agreement with the ISBT responsivity peak of the quantum wells [3] as predicted.

However, the precise wavelengths at R_{peak} for both etched and unetched detectors are 7.0 μm instead of the

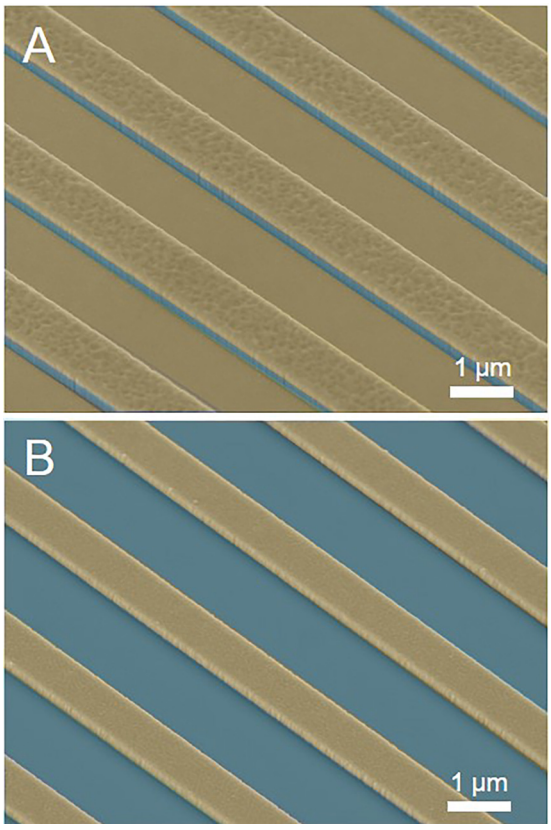

Figure 2: Colorized scanning electron microscope (SEM) images of A) etched and B) unetched detectors. Blue indicates the semiconductor region, gold indicates metallic regions. Images taken at 45° tilt angle.

predicted 6.7 μm; metasurface QWIPs have slightly red-shifted peaks compared with the original QWIP. Unexpected features can also be found in the peak height. The R_{peak} of 2.5 A/W observed for an unetched stripe detector (L = 0.85 μm) at a peak position of 7.0 μm is 8% higher than for any etched detector, with the closest value being 2.3 A/W at 7.0 μm for an etched detector with L = 1.06 μm (these representative specifications are summarized in Table 1). This result was surprising given the higher values of $|E_z|^2$ calculated for the etched cavities, which should correspond to greater absorption and responsivity. The lower R_{peak} for the etched detectors could indicate that some expected absorption in the etched cavities is not occurring, which is discussed in detail later.

Although we have been discussing their unpolarized R for enabling comparison with conventional photodetectors, stripe detectors still demonstrate strong polarization-dependent behavior as theoretically expected. As seen in Figure 3D, E, etched and unetched detectors selected for maximum R_{peak} (L = 1.06 μm and L = 0.85 μm, respectively) have over one order of magnitude difference in polarized responsivity respectively for φ = 0° ($R_{0°}$) and φ = 90° ($R_{90°}$).

Because the shift in R_{peak} wavelength compared with the original Brewster-angle detector (from 6.7 to 7.0 μm) occurs for all the stripe cavities irrespective of the etching, it may infer the presence of some changes in the quantum wells during the wafer bonding and the stripe fabrication, but before the final dry etching. This is discussed in more detail later in this manuscript. Also, we note the peak bias voltage (V_{peak}), the bias voltage that gives R_{peak}, was roughly 0.05 V lower for unetched detectors (0.44 V) than etched detectors (0.49 V, Table 1). The reason for this difference is not immediately apparent, but may arise from the electrical resistance of the detectors. In the unetched detectors, the current flowing between the Au stripes and

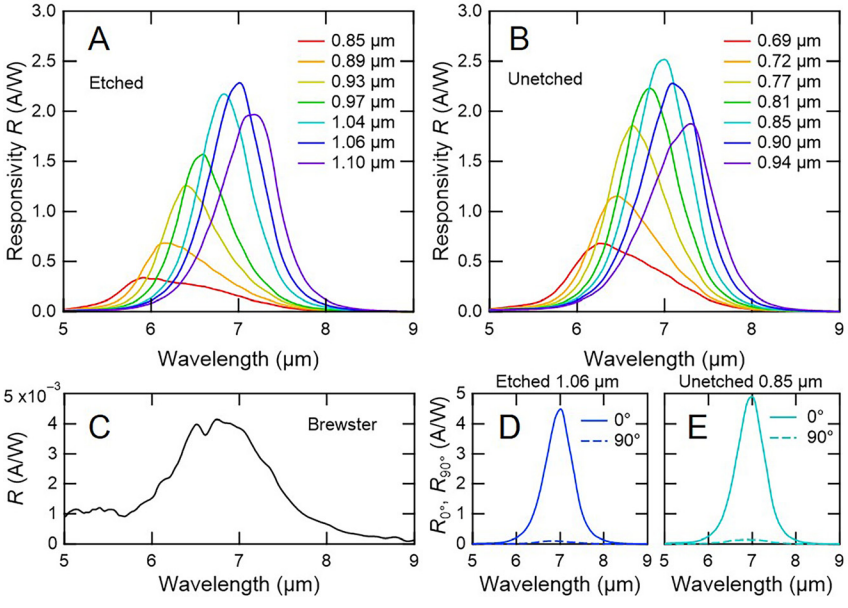

Figure 3: Experimental unpolarized responsivity spectra for A) etched and B) unetched detectors. Values of L cover the breadth of the quantum well absorption range. C) Brewster-angle detector spectrum used to determine range of L. D, E) Polarized responsivity for φ = 0° and 90° for representative etched and unetched detectors.

Table 1: Detector properties for etched and unetched stripe detectors from Figures 3D, E, and wired patch antennas from Ref. [6]. Values taken at conditions corresponding to R_{peak}.

	R_{peak} (A/W)	V_{peak} (V)	I_D (A)	I_{BG} (A)	$I_{P,\,BG}$ (A)	g	$D^*_D(cm\sqrt{Hz}/W)$	$D^*_{BG}(cm\sqrt{Hz}/W)$
Etched stripe	2.3	0.49	1.6×10^{-7}	2.9×10^{-7}	1.3×10^{-7}	2.6	4.3×10^{10}	3.3×10^{10}
Unetched stripe	2.5	0.44	4.0×10^{-7}	5.5×10^{-7}	1.5×10^{-7}	2.5	3.0×10^{10}	2.7×10^{10}
Etched patch	3.3	0.57	2.7×10^{-7}	4.8×10^{-7}	2.1×10^{-7}	2.3	5.2×10^{10}	3.9×10^{10}

the Au substrate can flow also through the unetched semiconductor layers. This could reduce the resistance of the detector with respect to other series resistance components so that the same electrical potential is applied to the quantum well at lower V_{peak}.

For infrared photodetectors, D^*, not R, is the fundamental figure of merit. Although higher R_{peak} was observed for unetched detectors, we cannot conclude their superiority to etched detectors until determining D^* based on other quantities. Before showing the definition of D^*, we would like to introduce photoconductive gain, which plays an important role in determining D^* and also in correlating ISBT absorption and R. The photoconductive gain (g) is the number of electrons circulating in a photoconductive detector per photoexcited electron generated in the quantum well [5, 7, 8]. Experimentally, we obtained g from dark current noise spectral density (see Section 4, Table 1). D^* can then be expressed by

$$D^*_D = R_{peak}\sqrt{\frac{A}{4egI_D}}, \tag{3}$$

in relation to R_{peak}, g, and I_D, where A is the device area and e is the electron charge. Because we discuss both I_D and I_{BG} in this manuscript, we consider both dark-current limited detectivity D^*_D, and background limited detectivity D^*_{BG} [7, 8], where for D^*_{BG}, I_{BG} simply replaces I_D. D^*_{BG} gives a practical detectivity for real-world application where the detector is exposed to environmental illumination.

Here we would like to discuss I_D, I_{BG}, and g. As seen in Figure 4A and Table 1, I_D is significantly reduced for the etched stripe detector compared to unetched detector in agreement with Chen et al. [3]. Similar behavior can be observed from I_{BG} in Table 1. The background photocurrent ($I_{P,BG}$), the contribution of photoexcited carriers to the background current I_{BG}, expressed as the difference between I_{BG} and I_D, for the etched detector ($I_{P,BG} = 1.3\times10^{-7}$ A) is slightly smaller than that for the unetched detector (1.5×10^{-7} A), nearly consistent with the relationship of the observed responsivity (R_{peak} = 2.3 A/W vs. 2.5 A/W). Figure 4B shows g as a function of bias voltage (Figure 4B). Note that g at V_{peak} is similar for both etched and unetched detectors (Table 1). Although g appears to be lower for the unetched stripe detectors in the bias range (0.4–0.7 V) in Figure 4B, the measurement accuracy of g is not necessarily high (0.3–0.5). Based on g measured for various etched, unetched, and Brewster-angle detectors [6], the difference found in Figure 4B should be considered insignificant, and we conclude that g is unique to the quantum well. Since g is similar for both detectors, $D^\star$ is greatly influenced by the current term.

Due to the degraded R for etched detectors, a delicate balance between reduced I_D and degraded R ultimately determines $D^\star$. As is summarized in Table 1, the etched stripe detector gives higher $D^\star$ both for D^*_D and D^*_{BG}, due to the reduced I_D and I_{BG}, demonstrating that the etched detector is superior to unetched detector. Because D^*_{BG} is lower than D^*_D for both detectors, they can be assumed to be operating in a background-limited regime at 78 K, which means that the I_D is sufficiently small at 78 K.

Quantitatively, D^*_{BG} for etched (3.3×10^{10} cm$\sqrt{\text{Hz}}$/W) and unetched stripe detctors (2.7×10^{10} cm$\sqrt{\text{Hz}}$/W) are close to the theoretical D^*_{BG} for an ideal photoconductive detector ($\sim 5\times10^{10}$ cm$\sqrt{\text{Hz}}$/W at 7 μm) [1]. Conventional HgCdTe detectors have nearly reached the theoretical limit. Therefore, our etched stripe detectors are approaching the level of state-of-the-art photodetectors at a similar wavelength range.

It is worth noticing that both stripe detectors show lower $D^\star$ values than the recently demonstrated wired patch antennas ($D^*_{BG} = 3.9\times10^{10}$ cm$\sqrt{\text{Hz}}$/W) [6]. From Table 1, first, low I_D for etched patch antennas similar to etched stripes is confirmed, indicating that etching reduces I_D regardless of cavity shape. However, we can also see that etched stripe detectors actually have lower I_D (1.6×10^{-7} A) than etched patch antennas (2.7×10^{-7} A) [6]. In contrast, R_{peak} of the patch antennas (3.3 A/W) is almost 1.5 times R_{peak} of the etched stripes (2.3 A/W), which compensates for the higher I_D. When designing cavities for higher D^*, the balance between I_D and R should be thus considered. The increased R in the etched patch antennas arises directly from the symmetry of the square patch design, as shown from φ-dependence measurements in Figure 4C. For both stripe detectors, polarized peak responsivities steadily

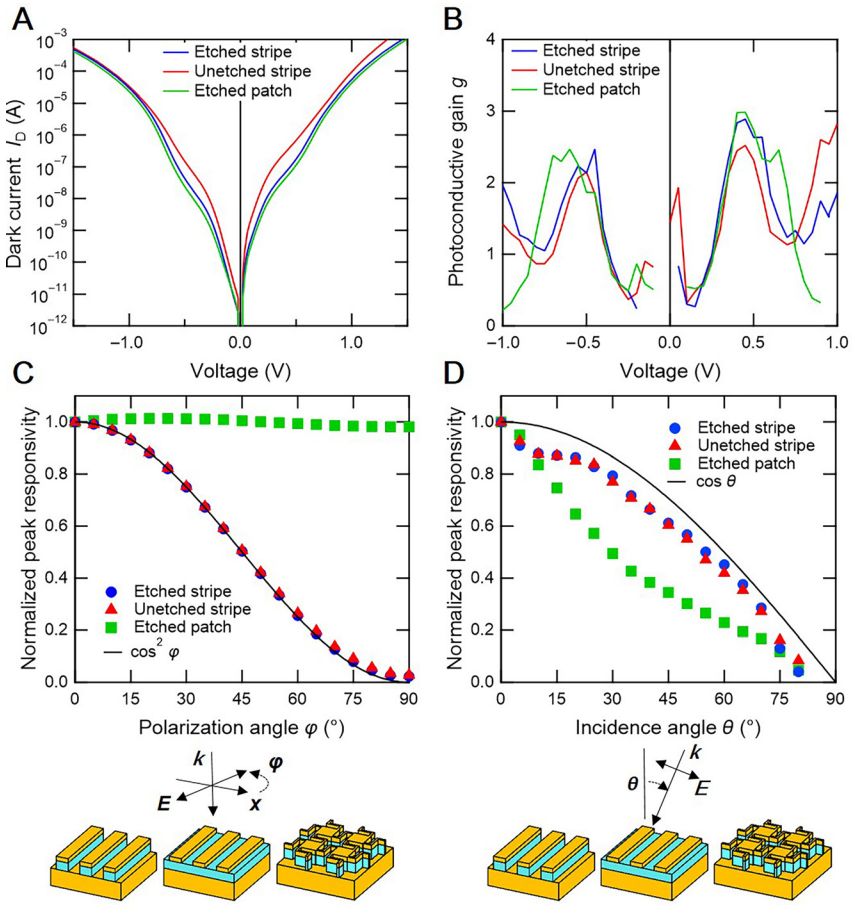

Figure 4: Device performance versus morphology for etched and unetched stripe detectors from Figure 3D, E and wired patch detector from Ref. [6]. A) Dark current I_D, B) photoconductive gain g, C) polarization angle-dependent R, and D) incidence angle-dependent unpolarized normalized R. Insets below C) and D) illustrate the geometry of the measurement. Etched patch detector schematic taken from Ref. [6], with patch length L = 1.19 μm, P = 2.0 μm, and thin Z-shape wires with width W = 100 nm and folding length S = 0.29 μm ***k*** and ***E*** indicate the incidence direction and polarization of incoming light.

decrease with increasing φ, following a characteristic $\cos^2 \varphi$ decay behavior previously observed in both stripe detectors [4] and square patch antennas connected by straight wires in stripe-like arrays [5]. In comparison, the two-dimensional symmetry of the wired patch antennas yields nearly constant R regardless of φ, and thus a higher unpolarized R_{peak}. Note that the larger background photocurrent ($I_{P,BG} = 2.1 \times 10^{-7}$ A) for the patch antennas confirms the more efficient light absorption of the square patch cavity shape.

The thin, etched wires used in the wired patch antennas were also reported to introduce angular dispersion [6] not found in the planar stripes or thin, unetched wires [3]. Incidence angle (θ) measurements taken by changing the angle of incident radiation in the x–z plane of the detectors are shown in Figure 4D (see schematic below graph). The normalized unpolarized R_{peak} of both stripe detectors shows a characteristic cos θ decay with increasing θ, indicating a large (~120°) detector field of view. In contrast, the dispersive wires in the wired patch antennas cause a more rapid R_{peak} decay, corresponding to a narrower (~60°) detector field of view which reduces the sensitivity of the detector to unwanted background radiation. Based on these results, we can see that a polarization-independent cavity design, particularly an etched structure, can offer improved R_{peak} along with reduced I_D and narrow fields of view. Because wired patch dimensions can be tuned according to the desired resonance wavelength, this design may be broadly applicable across many wavelengths.

In this work, there have been several unexpected observations: peak shift from the original Brewster-angle detector to the stripe detectors, and the inferior R of the etched stripe detectors. To discern changes in device performance originating from fabrication processes, experimental results were quantitatively compared with the simulations based on an exact model. The semiconductor layer was rigorously modeled as a five-layer dielectric structure made of a uniaxial quantum well, two barrier, and two contact layers (Section 4) [6], and L values for etched and unetched stripes were determined from SEM measurement of the actual specimens. The uniaxial dielectric function for the quantum well in this model was determined based on fitting to the responsivity spectrum of the Brewster-angle detector (Figure 3C). In comparison to the authors' previous report [6], the dielectric function used

in this manuscript was improved to better match the absorption profile of the quantum well (Figure 5A). Because ISBT absorption efficiency gives the generation probability of a photoexcited electron by ISBT per incident photon, this is equivalent to the internal quantum efficiency (IQE). We can experimentally determine the IQE for x polarization of our detectors from the measured R_{0° and g by the relation:

$$IQE(\lambda) = \frac{R_{0^\circ}(\lambda)}{\lambda g}\left(\frac{hc}{e}\right), \tag{4}$$

where λ, h, and c are wavelength, Planck's constant, and the speed of light, respectively.

We compare experimental IQE (solid lines) to the calculated ISBT absorption efficiencies (dashed lines) in Figure 5C, D. For easy comparison, we compare not the individual detectors, but the envelopes described by the profiles of the experimental and simulated spectra. The maxima of the experimental and simulated envelopes are indicated by horizontal black dotted lines. Differences in the peak height of each envelope are pronounced. We start with the unetched stripes (Figure 5D), in which etching effects do not appear. The maximum experimental IQE is 29% higher than the calculated absorption. Observing higher efficiency than calculated prediction is somewhat unusual and the underestimation of detector absorption suggests some change in the dielectric function of the quantum well. The Brewster-angle detector whose spectrum served as the basis for the dielectric function in this manuscript was fabricated while the quantum well was still on the initial lattice-matched GaAs substrate. In comparison, the quantum well in the stripe detectors has been transferred to an Au substrate, released from its original substrate, and sandwiched between the Au substrate and Au stripes. Any change in the strain state of the quantum well could change its optical properties. However, deeper discussion about the change in the quantum well properties is beyond the scope of this work.

The processing described above also occurs for the quantum well used for the etched stripe detector, so we would expect to see the same relation between IQE and the calculated absorption. As seen in Figure 5C, D, calculation (dashed lines) predicts higher absorption for etched stripes compared to unetched stripes, as has been shown by the simplified model (Figure 1D). Based on the above discussion assuming the change in the quantum well properties, much higher IQE is expected. Instead, the maximum experimental IQE for the etched stripes is 8% lower than calculation (Figure 5C), suggesting a large reduction in

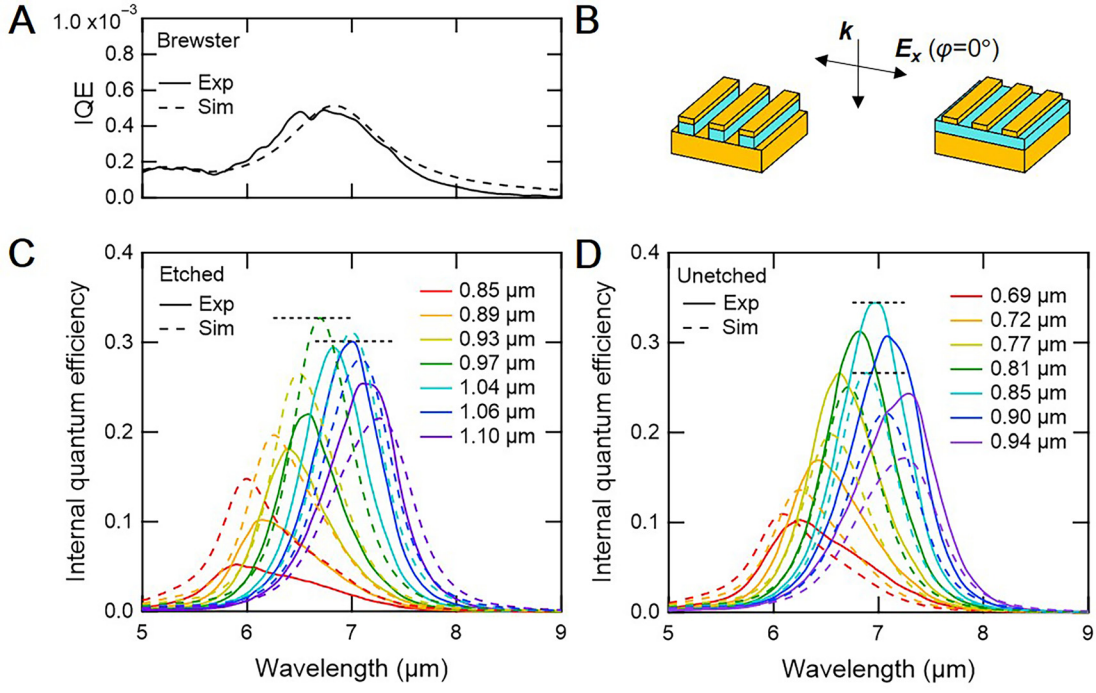

Figure 5: Experimental internal quantum efficiency (IQE) and simulated absorption efficiency in the stripe detectors (*x*-polarized). A) Brewster-angle detector experimental IQE and fit used to calculate the dielectric function for the quantum well. B) The illumination scheme shows incident light (***k***) and polarization (***x***) for all figures. Experimental IQE and simulated light absorption for C) unetched and D) etched cavities. The horizontal black dotted lines correspond to the maximum absorption in the experimental and simulated spectra.

absorption in our etched detectors. It is reasonable to assume that reduced IQE is a consequence of the etching, the only different process step during fabrication. Dry etching will lead to several changes in the semiconductor in the cavity, such as the formation of new GaAs/air and AlGaAs/air interfaces at the sidewalls. These are known to induce Fermi-level pinning and form depletion layers at the surfaces [28], which do not contribute to absorption. Damages due to the dry etching and oxidation could further compound this effect through trapping the electrons. Because $|E_z|^2$ is greatest near the cavity sidewall surfaces (See Figure 1D), depletion near the sidewalls could strongly degrade the responsivity.

Because QWIPs are unipolar devices, surface passivation and prevention of oxidation have typically been considered unnecessary [26]. However, the observed drastic decrease in the responsivity only for etched detectors suggests the etched surfaces are limiting device performance. Because etched metasurface QWIPs have a large surface area and absorption is strongest near the sidewall surfaces, the effects of etching should be considered in future designs. Simulations for predicting device performance should also consider these effects, as assuming pristine sidewalls may lead to significant overestimations.

Despite the reduced absorption, our etched stripe detectors still have higher D^* than unetched stripe detectors, and etched patch structures have the highest D^* in this study. Thus the benefits of I_D reduction from dry etching still outweigh the reduced R in the cavities. Promisingly, these results suggest that further improvement in the absorption, R, and D^* of etched metasurface QWIPs could be realized with appropriate sidewall surface treatments such as passivation or wet etching of damaged layers [29–32].

3 Conclusion

In summary, we have used a simple stripe cavity design to illustrate the fundamental features that lead to optimized device performance in metasurface QWIPs. Etching of exposed semiconductor material increases the magnitude of the electric field within the plasmon cavity due to the larger impedance mismatch between the cavity and the surrounding ambient. While this should promote stronger ISBT absorption, and greater R than in unetched cavities, experimental results showed that unetched cavities actually had slightly higher R_{peak} values. However, because dry etching strongly reduces I_D in the QWIPs, etched stripe detectors demonstrate higher D^*_D (both D^*_D and D^*_{BG}).

Detailed comparison of calculated absorption and experimental IQE in the quantum wells suggests that etched detectors suffer reduced absorption due to etching effects on the semiconductor at the cavity sidewalls. Nevertheless, etched structures show superior performance, which could be further improved with appropriate surface treatments. Through these experiments, we have clearly demonstrated how the shape and processing of different cavity morphologies drives metasurface QWIP performance. These results should be widely applicable for the design and fabrication of future metasurface QWIPs.

4 Methods

4.1 Quantum well design and fabrication

The QWIP structure was grown on n-GaAs (100) substrates (Si density: 1×10^{18} cm^{-3}) using a solid-source molecular beam epitaxy system. After the growth of a GaAs buffer layer, sacrificial (etch stop) layers of $Al_{0.9}Ga_{0.1}As$ (thickness: 900 nm, Si density: 5×10^{17} cm^{-3}) and $Al_{0.55}Ga_{0.45}As$ (100 nm, 5×10^{17} cm^{-3}) were grown. Then, an initial-side contact layer with a total thickness of 48 nm [20], consisting of a highly Si-doped GaAs layer (28 nm, 1.25×10^{19} cm^{-3}), a n-GaAs (15 nm, 3×10^{18} cm^{-3}), and a nondoped GaAs layer (5 nm), was grown. The main part of the QWIP is made of an $Al_{0.3}Ga_{0.7}As$ barrier (50 nm), an n-GaAs quantum well (4 nm, 3×10^{18} cm^{-3}, except for the final 0.85 nm), and an $Al_{0.3}Ga_{0.7}As$ barrier (50 nm). Finally, a 48-nm-thick end-side contact layer comprising a n-GaAs (20 nm, 3×10^{18} cm^{-3}) and a highly Si-doped GaAs layer (28 nm, 1.25×10^{19} cm^{-3}) was grown. To form the highly Si-doped GaAs layers, the growth of n-GaAs (28 nm, 5×10^{18} cm^{-3}) was interrupted and seven δ-doping layers of Si (3×10^{12} cm^{-2}) with a period of 4 nm were inserted. The layers from the initial-side contact to the end-side contact conform the QWIP layer to a total thickness of T = 200 nm. For this QWIP layer, the growth temperature was kept at relatively low 530 °C, which is important for realizing nonalloyed ohmic contact to the initial side.

4.2 Design, fabrication, and charcterization of Brewster-angle detectors

The intrinsic properties of the QWIP layer were evaluated by a Brewster-angle incidence detector which was fabricated from a small piece of the initial wafer. The Brewster-angle configuration exhibits a lower responsivity than the widely used back-illumination through a 45° facet, but its fabrication is easier. A Ti (bottom)/Au (top) electrode with a 100 × 400 μm aperture was patterned on top of a mesa defined by a H_2SO_4;H_2O_2:H_2O solution (1:8:1,000). For ohmic contact to the substrate side, an electrode made of Ni, AuGe, Ni, and Au was patterned on a wet-etched substrate surface and annealed at 420 °C for 90 s. Although the exact Brewster angle θ_B is 73°, the detector was set at $\theta_{B,exp}$ = 65° in the actual experiment due to the constraints of the

optical setup. This actual value was used in the calculation. This detector has sensitivity only for *p*-polarized incidence.

Because the quantum well was fabricated on a highly doped substrate, the measurement of the absorption spectrum by transmission was difficult. Therefore, the absorption spectrum was obtained from the responsivity spectrum of the Brewster-angle detector and the value of g (= 3.0) obtained from the noise measurement.

4.3 Fabrication of stripe detectors

The QWIP layer was coated with 3 nm-thick Ti and 150 nm-thick Au layers and bonded with another n-GaAs substrate coated with 10 nm-thick Ti and 500 nm-thick Au layers at a pressure of 5 MPa and a temperature of 250 °C for 60 min in N_2 atmosphere [33]. After mechanical polishing, the original GaAs substrate was chemically etched by a citric acid (1 g/mL):H_2O_2 solution (10:1) at 38 °C [34]. By etching the etch-stop AlGaAs layers using HF, the 200 nm-thick epitaxial QWIP layer was transferred onto an Au substrate.

Etched stripe detectors were fabricated on the transferred QWIP layer by electron-beam drawing and lift-off of 3 nm-thick Ti and 150 nm-thick Au top layers. Then, the specimen was coated with a 100 nm-thick SiO_2 film for electrical isolation. Windows of the SiO_2 layer were opened by dry etching using SF_6 around the detector areas. After patterning the electrode pads made of 3 nm-thick Ti and 150 nm-thick Au layers, so that one side can overlap with the edges of the stripe detector areas, the QWIP layers not covered by the upper Au stripes were vertically dry etched by inductively coupled plasma etching using Cl_2 and N_2 for etched detectors. The resultant Au layer after the dry etching was approximately 100 nm in thickness. For unetched detectors, the initial Au layer thickness was 100 nm, and no Cl_2 and N_2 etching of the semiconductor areas between the Au stripes was performed. For the patterning of the unetched stripe cavities, a laser-beam drawing method was used. Each detector is a 100 μm square and contains 41 stripes.

Note that for this QWIP layer, resistance across the semiconductor layers is dominated by the $Al_{0.3}Ga_{0.7}As$ barrier layers. Based on experimentally measured conductivity and mobility measurements [6], we can estimate that resistance in the barrier layers is several orders of magnitude larger than the GaAs contact layers and that the GaAs contact layers can be treated as perfect conductors. Therefore we can assume that any applied bias field across the detector is uniform across the entire area.

For efficient systematic evaluation, seven such detectors with different parameters were integrated on a chip and assembled on an 8-pin ceramic package. Another pin is for the common ground. The signals were extracted by bonding an Au wire at the root of each Au electrode.

4.4 Measurement of dimensions

Widths of the stripes L for the simulations were determined from SEM measurement. Because the period P is accurately defined by laser interferometry in the electron-beam drawing, L values were calibrated by the P values. In Figure 5C, D, there is a small peak discrepancy when comparing experimental and simulated curves for the same L value for both etched and unetched stripe detectors. These could be due to the distribution of the L values because their exact determination is not necessarily easy due to the tapered sidewalls of the stripes.

4.5 Measurement of optical properties

The detector was installed in a liquid-N_2 cryostat with ZnSe windows, and the responsivity spectra were measured with a FTIR spectrometer (JASCO, FT/IR-6200). The current from the detector was amplified (NF, CA5350) and fed into an external port of the FTIR. The spectral responsivity was quantified based on a calibrated HgCdTe detector. No corrections other than the detector areas were applied to the R values. The incident light from the FTIR was unpolarized. When necessary, a wire-grid polarizer was placed in the light path. The specimen in the cryostat was made to rotate around its vertical axis so that the incidence-angle dependence could be evaluated.

4.6 Measurement of electrical properties

To measure the dark current I_D, the detector was covered by a cold shield with a blackbody coating cooled at the same temperature as the detector (78 K). While a finite amount of blackbody radiation is emitted from the shield, it is sufficiently small. We can consider current measured under these conditions to be inherent to the detector. When the cold shield is removed, a background light at 298 K is incident on the detector from an area with an effective field of view of 102°. The current–voltage relationship was measured with a source meter (Keithley, 2635B).

The value of gain g was determined from I_D, and noise spectral density $i_n/\Delta f^{1/2}$ (Δf: bandwidth) measured by a fast Fourier transform analyzer (Ono Sokki, CF-4700), by the relationship $i_n/\Delta f^{1/2} = (4egI_D)^{1/2}$. The value at 1 kHz was used [35].

4.7 Electromagnetic simulation and design of stripe detectors

For the rigorous analysis shown in Figure 5, and the Fresnel equations for the Brewster-angle detector, where an accurate vertical electric field at the quantum well layer is necessary for obtaining R, the QWIP layer was treated as a wavelength-dependent five-layer multilayer. The quantum well was assumed as a uniaxial material with ISBT absorption in the vertical direction and free-carrier absorption in the lateral directions.

The wavelength-dependent refractive indices of the nondoped GaAs and $Al_{0.3}Ga_{0.7}As$ were based on Palik [36]. To express the free-carrier absorption, a Drude term $-\omega_p^2/(\omega^2 + i\gamma\omega)$ was added, where ω_p and $1/\gamma$ are the plasma frequency and relaxation time, respectively [37], both of which are specified by the carrier density, N, and mobility, μ, respectively [19]. The contact layer was regarded as an isotropic Drude material corresponding to experimentally obtained $N = 4.7 \times 10^{18}$ cm^{-3} and $\mu = 1500$ cm^2/(Vs). For the lateral directions of the quantum well layer, a Drude term corresponding to the experimental $N = 2.4 \times 10^{18}$ cm^{-3} and $\mu = 2000$ cm^2/(Vs) was considered. In the vertical direction of the quantum well layer, the ISBT absorption was described with a three-term Lorentzian model [13], considering the term $-\Omega_{pj}^2/(\omega^2 - \Omega_j^2 + i\Gamma_j\omega)$ (j = 1, 2, and 3). We set (Ω_1, Γ_1, Ω_{p1}) = (158, 30, 304), (Ω_2, Γ_2, Ω_{p2}) = (236, 39, 114), and (Ω_3, Γ_3, Ω_{p3}) = (279, 73, 124) in meV. These values were obtained initially by Fermi's golden rule [19] and then by making a small correction to j = 1, so that the values yielded consistent results with the experimental R of the Brewster-angle detector (see Figure 5A).

Acknowledgments: The authors acknowledge helpful discussion with an anonymous company, H. Miyazaki, Y. Jimba, Y. Sakuma, T. Noda, A. Ohtake, D. Tsuya, N. Ikeda, E. Watanabe, K. Miyano, M. Iwanaga, and K. Sakoda. This work was supported by JSPS KAKENHI Grant Numbers JP15H02011, JP17H01275, and JP19H00875, Iketani Science and Technology Foundationgs, the Center for Functional Sensors and Actuators, the National Institute for Materials Science (NIMS), and the NIMS Nanofabrication Platform in Nanotechnology Platform Project sponsored by the Ministry of Education, Culture, Sports, Science and Technology, Japan.

Author contribution: All the authors have accepted responsibility for the entire content of this submitted manuscript and approved submission.

Research funding: Funded by Japan Society for the Promotion of Science, JP15H02011, JP17H01275, JP19H00875; Iketani Science and Technology Foundation Japan; Center for Functional Sensors and Actuators; National Institute for Materials Science Japan; Ministry of Education, Culture, Sports, Science and Technology Japan.

Conflict of interest statement: The authors declare no conflicts of interest regarding this article.

References

[1] A. Rogalski. "History of infrared detectors." *Opto-Electronics Rev.*, vol. 20, no. 3, pp. 279–308, 2012.

[2] M. Kopytko and A. Rogalski. "HgCdTe barrier infrared detectors." *Prog. Quant. Electron.*, vol. 47, pp. 1–18, 2016.

[3] Y. Nga Chen, Y. Todorov, B. Askenazi, et al., "Antenna-coupled microcavities for enhanced infrared photo-detection." *Appl. Phys. Lett.*, vol. 104, no. 3, p. 031113, 2014.

[4] Q. Li, Z. Li, N. Li, et al., "High-polarization-discriminating infrared detection using a single quantum well sandwiched in plasmonic micro-cavity." *Sci. Rep.*, vol. 4, no. 1, p. 6332, 2015.

[5] D. Palaferri, Y. Todorov, A. Bigioli, et al., "Room-temperature nine-μm-wavelength photodetectors and GHz-frequency heterodyne receivers." *Nature*, vol. 556, no. 7699, pp. 85–88, 2018.

[6] H. T. Miyazaki, T. Mano, T. Kasaya, et al., "Synchronously wired infrared antennas for resonant single-quantum-well photodetection up to room temperature." *Nat. Commun.*, vol. 11, no. 565, 2020, https://doi.org/10.1038/s41467-020-14426-6.

[7] B. F. Levine. "Quantum-well infrared photodetectors." *J. Appl. Phys.*, vol. 74, no. 8, pp. R1–R81, 1993.

[8] H. Schneider and H. C. Liu. Quantum Well Infrared Photodetectors, Berlin, Germany, Springer, 2007.

[9] G. Lévêque and O. J. F. Martin. "Tunable composite nanoparticle for plasmonics." *Opt. Lett.*, vol. 31, no. 18, pp. 2750–2752, 2006.

[10] H. T. Miyazaki and Y. Kurokawa. "Squeezing visible light waves into a 3-nm-Thick and 55-nm-Long plasmon cavity." *Phys. Rev. Lett.*, vol. 96, no. 9, p. 097401, 2006.

[11] J. Le Perchec, Y. Desieres, and R. Espiau De Lamaestre. "Plasmon-based photosensors comprising a very thin semiconducting region." *Appl. Phys. Lett.*, vol. 94, no. 18, p. 181104, 2009.

[12] H. T. Miyazaki and Y. Kurokawa. "How can a resonant nanogap enhance optical fields by many orders of magnitude?." *IEEE J. Sel. Top. Quant. Electron.*, vol. 14, no. 6, pp. 1565–1576, 2008.

[13] C. F. Bohren , D. R. Huffman. *Absorption and Scattering of Light by Small Particles*. New York: Wiley; 1983.

[14] D. Palaferri, Y. Todorov, A. Mottaghizadeh, G. Frucci, G. Biasiol, and C. Sirtori. "Ultra-subwavelength resonators for high temperature high performance quantum detectors." *New J. Phys.*, vol. 18, no. 11, p. 113016, 2016.

[15] X. Liu, T. Starr, A. F. Starr, and W. J. Padilla. "Infrared spatial and frequency selective metamaterial with near-unity absorbance." *Phys. Rev. Lett.*, vol. 104, no. 20, p. 207403, 2010.

[16] I. Puscasu and W. L. Schaich. "Narrow-band, tunable infrared emission from arrays of microstrip patches." *Appl. Phys. Lett.*, vol. 92, no. 23, p. 233102, 2008.

[17] Y. H. Ye, Y. W. Jiang, M. W. Tsai, et al., "Localized surface plasmon polaritons in Ag/SiO_2/Ag plasmonic thermal emitter." *Appl. Phys. Lett.*, vol. 93, no. 3, p. 033113, 2008.

[18] H. T. Miyazaki, T. Kasaya, H. Oosato, et al., "Ultraviolet-nanoimprinted packaged metasurface thermal emitters for infrared CO_2 sensing." *Sci. Technol. Adv. Mater.*, vol. 16, no. 3, p. 035005, 2015.

[19] J. H. Davies. *The Physics of Low-Dimensional Semiconductors*, Cambridge, Cambridge University Press, 1997.

[20] T. Mano, H. T. Miyazaki, T. Kasaya, T. Noda, and Y. Sakuma. "Double-sided nonalloyed ohmic contacts to Si-doped GaAs for plasmoelectronic devices." *ACS Omega*, vol. 4, no. 4, pp. 7300–7307, 2019.

[21] R. Gordon. "Light in a subwavelength slit in a metal: propagation and reflection." *Phys. Rev. B – Condens. Matter Mater. Phys.*, vol. 73, no. 15, p. 153405, 2006.

[22] S. Collin, F. Pardo, and J.-L. Pelouard. "Waveguiding in nanoscale metallic apertures." *Opt. Express*, vol. 15, no. 7, pp. 4310–4320, 2007.

[23] Y. Todorov, A. M. Andrews, I. Sagnes, et al., "Strong light-matter coupling in subwavelength metal-dielectric microcavities at terahertz frequencies." *Phys. Rev. Lett.*, vol. 102, no. 18, p. 186402, 2009.

[24] Y. Todorov, L. Tosetto, J. Teissier, et al., "Optical properties of metal-dielectric-metal microcavities in the THz frequency range." *Opt. Express*, vol. 18, no. 13, pp. 13886–13907, 2010.

[25] J. Yang, C. Sauvan, A. Jouanin, S. Collin, J.-L. Pelouard, and P. Lalanne. "Ultrasmall metal-insulator-metal nanoresonators: impact of slow-wave effects on the quality factor." *Opt. Express*, vol. 20, no. 15, pp. 16880–16891, 2012.

[26] A. Nedelcu, C. Bonvalot, R. Taalat, et al., III-V detector technologies at Sofradir: dealing with image quality. *Infrared Phys. Technol.*, vol. 94, p. 273–279, 2018.

[27] M. A. Ordal, R. J. Bell, R. W. Alexander, L. L. Long, and R. M. R. Querry. "Optical properties of Au, Ni, and Pb at submillimeter wavelengths." *Appl. Opt.*, vol. 26, no. 4, pp. 744–752, 1987.

[28] S. M. Sze and K. K. Ng. Physics of Semiconductor Devices, Hoboken, NJ, USA, John Wiley & Sons, 2006.

[29] B. Corbett and W. M. Kelly. "Surface recombination in dry etched AlGaAs/GaAs double heterostructure p-i-n mesa diodes." *Appl. Phys. Lett.*, vol. 62, no. 1, pp. 87–89, 1993.

[30] S. W. Pang. "Surface damage on GaAs induced by reactive ion etching and sputter etching." *J. Electrochem. Soc.*, vol. 133, no. 4, pp. 784–787, 1986.

[31] D. Englund, H. Altug, and J. Vučković. "Low-threshold surface-passivated photonic crystal nanocavity laser." *Appl. Phys. Lett.*, vol. 91, no. 7, p. 071124, 2007.
[32] K. Kuruma, Y. Ota, M. Kakuda, S. Iwamoto, and Y. Arakawa. "Surface-passivated high-Q GaAs photonic crystal nanocavity with quantum dots." *APL Photon.*, vol. 5, no. 4, p. 046106, 2020.
[33] B. S. Williams, S. Kumar, Q. Hu, and J. L. Reno. "Operation of terahertz quantum-cascade lasers at 164 K in pulsed mode and at 117 K in continuous-wave mode." *Opt. Express*, vol. 13, no. 9, pp. 3331–3339, 2005.
[34] A. R. Clawson. "Guide to references on III-V semiconductor chemical etching." *Mater. Sci. Eng. R Rep.*, vol. 31, no. 1–6, pp. 1–438, 2001.
[35] B. F. Levine, C. G. Bethea, G. Hasnain, et al., "High sensitivity low dark current 10 μm GaAs quantum well infrared photodetectors." *Appl. Phys. Lett.*, vol. 56, no. 9, pp. 851–853, 1990.
[36] E. D. Palik. *Handbook of Optical Constants of Solids*. San Diego, CA, USA: Academic Press; 2012.
[37] S. A. Maier. *Plasmonics: Fundamentals and Applications*, New York, NY, USA: Springer; 2004.